

The Effect of Initial Defects on Overall Mechanical Properties of Concrete Material

Yunfa Zhang¹, Xiaozhou Xia^{1,*}, Zhenjie Wu¹ and Qing Zhang¹

Abstract: Considering the fact that the initial defects, like the imperfect interfacial transition zones (ITZ) and the micro voids in mortar matrix, weaken the mechanical properties of concrete, this study develops corresponding constitutive models for ITZ and matrix, and simulates the concrete failure with finite element methods. Specifically, an elastic-damage traction-separation model for ITZ is constructed, and an anisotropic plastic-damage model distinguishing the strength-difference under tension and compression for mortar matrix is proposed as well. In this anisotropic plastic-damage model, the weakening effect of micro voids is reflected by introducing initial isotropic damage, the distinct characteristic of tension and compression which described by decomposing damage tensor into tensile and compressive components, and the plastic yield surface which established on the effective stress space. Furthermore, by tracking the damage evolution of concrete specimens suffering uniaxial tension and compression, the effects of imperfect status of ITZ and volume fraction of initial voids on the concrete mechanical properties are investigated.

Keywords: Imperfect ITZ, initial voids, anisotropic plastic-damage constitutive, meso-scale concrete.

1 Introduction

Concrete can be taken as a multi-phase composite material consisting of mortar matrix, aggregates, micro defects, and interfacial transition zone (ITZ) between the aggregates and the mortar matrix. Its macro mechanical characteristics are determined by the microstructural features (e.g., aggregate shape, size, gradation, and distribution, ITZ thickness and mechanical properties, the mortar matrix mechanical properties, voids fraction and distribution, etc.). So, it is important to bridge the microstructure-property relationship for designing better and superior fracture-resistant cementitious materials. In order to better grasp the concrete mechanical properties, micromechanical model reflecting the inelastic and damage behavior of each phase is crucial. For ITZ, its mechanical characteristics, like connecting status, stiffness and strength play an important role in the concrete fracture behavior [Ollivier, Maso and Bourdette (1995)]. For mortar matrix, its mechanical properties, like the distinct tensile and compressive characteristic,

¹ Department of Engineering Mechanics, Hohai University, Nanjing, 210098, China.

* Corresponding Author: Xiaozhou Xia. Email: xiaxiaozhou@163.com.

devotes the determinate contribution to concrete mechanical properties. And for aggregates, its volume fraction and gradation determinate the hardening and softening characteristic of concrete. What's more, the initial voids in mortar matrix reduce the stiffness and strength to some extent. If these voids are considered in discretization, the computational cost of three-dimensional modeling will be more expensive [Yin, Yang and Yang (2013); Al-Rub and Kim (2010)]. Therefore, homogenizing the mortar paste to reflect the weakening effect of initial voids is a best treatment. Due to the recent advances Idiart et al. [Idiart, López and Carol (2011)] in capturing the composition, porosity and strength of the ITZ and mortar matrix, and the developments in computational power and improvements of computational software [Talebi, Silani, Bordas et al. (2014)], one can effectively simulate the micromechanical behavior of concrete materials. Therefore, this study will focus on conducting a desirable numerical concrete model at the meso-scale and constructing reasonable constitutive model considering the reduction effect of initial defects for the ITZ and mortar matrix.

The implementation process of the meso-scale modeling of concrete can be categorized mainly into two steps. First step is to generate aggregates taking into account the shape, distribution, and their volume fraction, and second step is to perform a simulation with numerical model, i.e., FEM, XFEM [Moës and Belytschko (2002)], XEFG [Rabczuk and Belytschko (2007); Rabczuk, Bordas and Zi (2010)], applying constitutive models to each phase. Although various generation techniques of particles Sun et al. [Sun (2005); Bažant, Tabbara, Kazemi et al. (1990); Fu and Dekelbab (2003); Wang, Yang and Jivkov (2015)] have been proposed for concrete on meso level, the corresponding mesh generation is still a trivial thing, which the main trouble is that it is hard to mesh all the particles with different sizes and shape in a several unified plannings. A more suitable method avoiding the difficulty of directly meshing particles is the grid mapping scheme [Fang, Zhang, Huan et al. (2013)] in which only judges the mapping region of each phase based on a regular mesh. To ensure the accuracy, the grid of mesh have to be very small to suit the irregular surface of aggregate, which cause to the huge computational cost. For the real micro-structure model reformed from the X-ray scanned pictures, Huang et al. [Huang, Yang, Ren et al. (2015)] adopt the grid mapping model where the size of each grid is the same as the pixel size to simulate the fracture-damage process of concrete. To avoid the complicated meshing of the particles and mortar matrix, the lattice beam model Schlangen et al. [Schlangen and Garboczi (1997); Van Mier (2017); Lilliu and van Mier (2003)] and Lattice discrete particle model Cusatis et al. [Cusatis, Pelessone and Mencarelli (2011); Cusatis, Mencarelli, Pelessone et al. (2011)] are proposed. Another approach of microscopic numerical simulation for concrete is the random mechanical model [Zhu and Tang (2002); Zhu, Teng and Tang (2004)] in which no aggregate needs to be generated.

As described above, the accurate reflection of mechanical properties of ITZ is crucial. In lattice beam model Schlangen et al. [Schlangen and Garboczi (1997); Van Mier (2017); Lilliu and Van Mier (2003)], the thickness of ITZ is wider than the actual thickness (at least 10 times as large as the real ITZ), and the complex mechanical behavior of ITZ is hard to reflect on the beam lattice. However, the embedded cohesive elements in FEM Wang et al. [Wang, Yang and Jivkov (2015); Su, Yang and Liu (2010); Gálvez, Planas, Sancho et al. (2013)] or the embedded cohesive crack in XFEM [Moës and Belytschko

(2002); Fang, Xia and Zhang (2018)], XEFG [Rabczuk, Zi, Bordas et al. (2008); Rabczuk, Bordas and Zi (2010)] and cracking-particle method [Rabczuk, Zi, Bordas et al. (2010); Rabczuk and Belytschko (2004)] can well reflect the real mechanical behavior of ITZ by setting the thickness parameter and assigning the reasonable constitutive model under the framework of traction-separation relation. Most of the cracking criteria in the cohesive model are defined at the traction space, such as the quadratic nominal stress criterion Wang et al. [Wang, Yang and Jivkov (2015)], the Mohr-Coulomb criterion Fang et al. [Fang, Xia and Zhang (2018)] and various modified Mohr-Coulomb criterion [Rabczuk, Zi, Bordas et al. (2008)]. There are also some cracking initialization criteria based on the maximal strain or the equivalent energy release rate [Rabczuk, Zi, Bordas et al. (2010)]. Before the interface damage occurs, the traction is linear with the separation. Once the damage happens in ITZ, it will develop along the gradient direction of the dissipative potential, and its magnitude can be determined by the consistency condition. Usually, the traction-separation relationship for pure tension and pure shear are given in advance, where the soften section of the traction-separation curves can be determined by the fractured and slipped energy release rate of ITZ and corresponding energy release mode, such as linear Wang et al. [Wang, Yang and Jivkov (2015)], bilinear Su et al. [Su, Yang and Liu (2010)] and exponential mode Nakamura et al. [Nakamura, Srisoros, Yashiro et al. (2006)]. The damage evolution curve can also be calibrated by equivalent relative displacement or surface energy density [Benzeggagh and Kenane (1996)]. Though the damage softening surface is probably not same as the dissipation potential face at the compression-shear area because of the dilation effect [Ferté, Massin and Moës (2016); Carol, Prat and Lopez (1997)], the symmetric of matrix can be still kept because of no Poisson's effect. It is worth mentioning that the rigid-body-spring method [Rabczuk, Zi, Bordas et al. (2008); Zhuo and Zhang (2000)] can also reflect the mechanical behavior of ITZ, but the deformation of matrix is neglected. What's more, if the ITZ is taken as zero thickness interface, the traction-separation relation presents initially rigid linear, bilinear or exponential softening mode [Rabczuk, Bordas and Zi (2010)].

For the mortar matrix, its mechanical properties are similar to the concrete due to the sand playing a role of aggregate. So, the constitutive model of concrete can be used to simulate the mechanical behavior of mortar matrix by setting different parameters from that of concrete. One of the most important characteristics is its low tensile strength, particularly at low-confining pressures, which results in tensile cracking and further leads to the reduction of the stiffness along perpendicular direction to the crack. What's more, the mortar matrix undergoes also irreversible plastic deformations dedicated by the paste cement phase. That is, the nonlinear material behavior of mortar matrix can be attributed to two distinct mechanical processes: damage (micro-cracks, micro-cavities, nucleation and coalescence, decohesions, grain boundary cracks) and plasticity. These two degradation phenomena may be best described by theories of continuum damage mechanics and plasticity [Cicekli, Voyiadjis and Al-Rub (2007)]. Therefore, a model that accounts for both plasticity and damage is necessary.

In this manuscript, the aggregates in concrete are assumed to keep not fracture or damage in whole loading process. On the base of plastic-damage model proposed by Cicekli et al. [Cicekli, Voyiadjis and Al-Rub (2007)], the weakening effect of initial voids on overall

properties of mortar matrix is considered by introducing the initial isotropic damage. Specifically, the random distributed voids are smeared into the concrete uniformly, and the degradation effect on the overall stiffness of concrete material can be evaluated by the micro-mechanics theory [Mura (2013)]. While the reduction effect of carrying capacity induced by initial voids can be reflected by constructing the effective stress based plastic yield surface. The involving model parameters for mortar matrix refer to the literature [Kim and Al-Rub (2011)].

This paper is organized as follows: we will present the traction-separation law for ITZ that takes its initial imperfect status into account and the anisotropic plastic-damage model for mortar matrix that considers the weakening effect of initial voids in Sections 2 and 3. In Section 4, we will establish the FEM for concrete at the meso-scale, which involves the cohesive element for ITZ, governing equations and its integral weak form, domain discretization, generation of random distributed aggregates and mesh of concrete specimen. In Section 5, we will verify the validity of the proposed model. And the effect of the volume fraction of initial void, the ITZ stiffness and strength on the overall mechanical properties of concrete will be investigated in the Section 6. Finally, summary and some conclusions of this research are presented in the Section 7.

2 Elastic-damage model for imperfect ITZ

Due to the fact that the thickness h of ITZ is very smaller and less than a tenth of aggregate, it is unfitted to mesh the ITZ by using solid element, which results in a huge mesh scale. In this study, the cohesive element is used to discretize the ITZ. Therefore, the original three-phase configuration of concrete with ITZ should be simplified two-phase configuration, as presented in Fig. 1. So the ITZ constitutive law should be established on the framework of traction-separation relation.

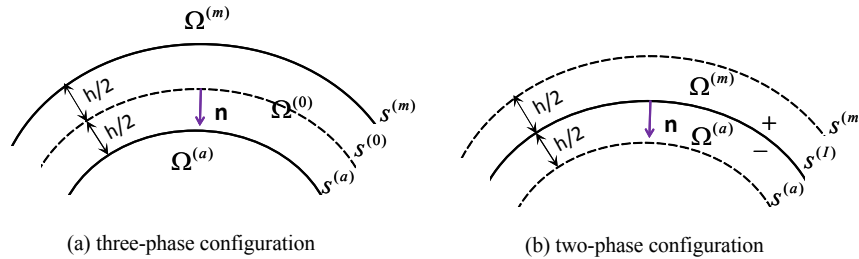


Figure 1: Modelling of an ITZ in a three-phase configuration as an imperfect ITZ in a two-phase configuration

The traction $\mathbf{t}_{coh} = \{\sigma_n \quad \tau_s \quad \tau_t\}^T$ in the ITZ can be defined as the function of open displacement $[\mathbf{u}'] = \{[u_n] \quad [u_s] \quad [u_t]\}^T$ or the strain at the ITZ $\boldsymbol{\varepsilon}_{coh} = \{\varepsilon_n \quad \varepsilon_s \quad \varepsilon_t\}^T$, such that

$$\begin{Bmatrix} \sigma_n \\ \tau_s \\ \tau_t \end{Bmatrix} = - \begin{bmatrix} K_n^0(1-d_n^0)(1-d_n) & 0 & 0 \\ 0 & K_s^0(1-d_s^0)(1-d_s) & 0 \\ 0 & 0 & K_t^0(1-d_t^0)(1-d_t) \end{bmatrix} \begin{Bmatrix} [u_n] \\ [u_s] \\ [u_t] \end{Bmatrix} \quad (1)$$

$$\Rightarrow \mathbf{t}_{coh} = -\mathbf{D}_{coh}[\mathbf{u}'] = -h\mathbf{D}_{coh}\boldsymbol{\varepsilon}_{coh}$$

where \mathbf{D}_{coh} is the elastic-damage matrix, d_n^0, d_s^0, d_t^0 are the initial damages of normal and two shear direction respectively, which reflect the initial connect status of ITZ. d_n, d_s, d_t are the damages of normal and two shear direction at the ITZ respectively, K_n^0, K_s^0, K_t^0 are the initial interfacial stiffness along normal and two tangential direction respectively, $[u_n], [u_s], [u_t]$ are the relative displacement of normal and two tangential direction at the ITZ respectively. In this study, the effect of initial damage is considered and the bilinear curves are adopted to describe the traction-separation relation along the normal and shear direction as shown in Fig. 2 and Fig. 3. Assuming the ITZ is of the same behavior for two tangential direction, the damage evolution equation can be derived from formula (1) as follows

$$d_n = \frac{[u_n^s]([u_n] - [u_n^{0'}])}{[u_n]([u_n^s] - [u_n^{0'}])}, \quad d_t = \frac{[u_t^s]([u_t] - [u_t^{0'}])}{[u_t]([u_t^s] - [u_t^{0'}])} = d_s \quad (2)$$

where $[u_n^{0'}], [u_t^{0'}]$ are the relative displacements along normal and shear direction corresponding to the maximum traction respectively considering the initial damage of ITZ, such that

$$[u_n^{0'}] = \frac{[u_n^s][u_n^0]}{[u_n^s] - d_n^0([u_n^s] - [u_n^0])}, \quad [u_t^{0'}] = \frac{[u_t^s][u_t^0]}{[u_t^s] - d_t^0([u_t^s] - [u_t^0])} \quad (3)$$

where $[u_n^0], [u_t^0]$ are the relative displacements along normal and shear direction corresponding to the maximum traction respectively, and $[u_n^s], [u_t^s]$ are the open and slide displacement corresponding to traction free status respectively.

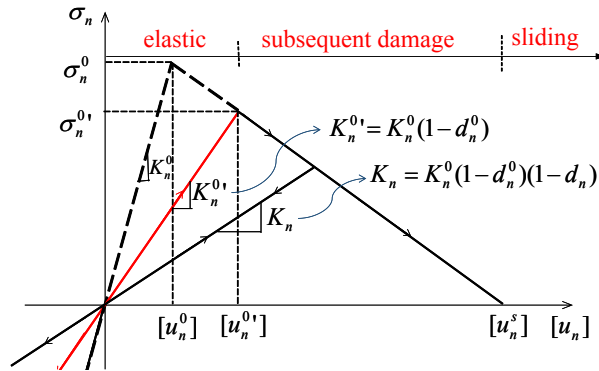


Figure 2: The relationship between the normal traction and normal separation considering the initial damage

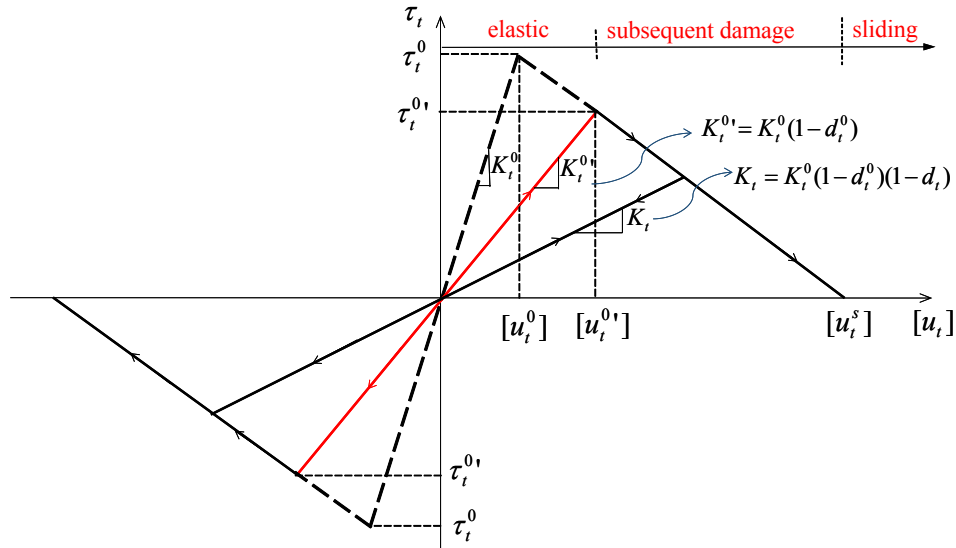


Figure 3: The relationship between the shear traction and shear separation considering the initial damage

The quadratic stress criterion as following formula is used to judge whether the initial damage does occur.

$$f = \left\{ \frac{\langle \sigma_n \rangle}{\sigma_n^{0'}} \right\}^2 + \left\{ \frac{\tau_s}{\tau_s^{0'}} \right\}^2 + \left\{ \frac{\tau_t}{\tau_t^{0'}} \right\}^2 - 1 \quad (4)$$

where $\sigma_n^{0'}$, $\tau_s^{0'}$, $\tau_t^{0'}$ are the critical stress of normal and two shear direction corresponding to initial damage status separately. ' $\langle \rangle$ ' is the operator defined as follows

$$\begin{cases} \langle x \rangle = x & \text{when } x > 0 \\ \langle x \rangle = 0 & \text{when } x \leq 0 \end{cases} \quad (5)$$

3 The coupled anisotropic plastic-damage constitutive model considering initial damage for mortar matrix

3.1 Modeling the initial damage and anisotropic damage in mortar matrix

Generally, mortar matrix contains some micro holes which are difficult to simulate in real geometric configuration due to the very small size of them. Therefore, adopting the framework of continuum mechanics and taking these micro holes as initial damage is the best choice to model the mechanical behavior of mortar matrix with micro holes. Assume the shapes of these micro holes in it are all sphere and the mortar matrix are isotropic. The overall bulk modulus K and shear modulus G can be derived respectively as follows by utilizing sparse estimation method [Kim and Al-Rub (2011)]:

$$\begin{cases} K = \bar{K}[1-c][1 + \frac{c\alpha^E}{1-\alpha^E}]^{-1} \\ G = \bar{G}[1-c][1 + \frac{c\beta^E}{1-\beta^E}]^{-1} \end{cases} \quad (6)$$

where c is the volume content of micro-hole defects, \bar{K} and \bar{G} are the bulk and shear modulus respectively of undamaged mortar matrix with no any micro hole, and α^E, β^E are the Eshelby isotropic parameters for sphere cavity inclusion, which are gained as follows [Kim and Al-Rub (2011)]:

$$\alpha^E = \frac{3\bar{K}}{3\bar{K} + 4\bar{G}} = \frac{1 + \bar{\nu}}{3(1 - \bar{\nu})}, \beta^E = \frac{6(\bar{K} + 2\bar{G})}{5(3\bar{K} + 4\bar{G})} = \frac{2(4 - 5\bar{\nu})}{15(1 - \bar{\nu})} \quad (7)$$

It can be seen from expression (6) that the initial damage effect of micro holes on the overall mechanics of mortar matrix is isotropic. Therefore, the overall evaluation formula (6) can be rewritten as the damage form

$$\begin{cases} K = \bar{K}[1 - d^+] \\ G = \bar{G}[1 - d^-] \end{cases} \quad (8)$$

where d^+ and d^- are the initial damage varies gained as follows

$$\begin{cases} d^+ = \frac{c}{1 - \alpha^E + c\alpha^E} \\ d^- = \frac{c}{1 - \beta^E + c\beta^E} \end{cases} \quad (9)$$

According the static equivalent principle, the normal stress σ_{ij} can be expressed by effective stress $\bar{\sigma}_{ij}$ as follows

$$\sigma_{ij} = M'_{ijkl} \tilde{\sigma}_{kl} = M'_{ijmn} M^0_{mnkl} \bar{\sigma}_{kl} = M_{ijkl} \bar{\sigma}_{kl} \quad (10)$$

where $\tilde{\sigma}_{ij}$ is the initial effective stress, M^0_{ijkl} is the fourth-order initial damage effect tensor which can be taken as isotropic tensor by the formula (8)

$$M^0_{ijkl} = (1 - d^-) \delta_{ik} \delta_{jl} + [(1 - d^+) - (1 - d^-)] \frac{1}{3} \delta_{ij} \delta_{kl} \quad (11)$$

and M'_{ijkl} is the fourth-order damage effect tensor defined as follows [Al-Rub and Voyiadjis (2003); Voyiadjis and Park (1997)]:

$$M'_{ijkl} = \frac{1}{2} [(\delta_{ik} - \varphi_{ik}) \delta_{jl} + \delta_{il} (\delta_{jk} - \varphi_{jk})] \quad (12)$$

where φ_{ij} is the damage tensor and δ_{ij} is the Kronecker delta. When no damage occurs, that is $\varphi_{ij} = 0$, the damage effect tensor M'_{ijkl} become back to the fourth-order identity tensor

$$M'_{ijkl} |_{\varphi_{ij}=0} = I_{ijkl} = \frac{1}{2}(\delta_{ik}\delta_{jl} + \delta_{il}\delta_{jk}) \quad (13)$$

The transformation from the effective (undamaged) configuration to the damaged one can be done by utilizing the strain equivalence hypotheses [Voyiadjis (2012)], which states that the strains in the damaged configuration and the strains in the undamaged (effective) configuration are equal. Therefore, the damaged elasticity tensor E_{ijkl} can be expressed by the corresponding undamaged elasticity tensor \bar{E}_{ijkl} as follows:

$$E_{ijkl} = M_{ijmn} \bar{E}_{mnlk} \quad (14)$$

where the undamaged elastic tensor \bar{E}_{ijkl} can be expressed by effective shear modulus \bar{G} and buck modulus \bar{K} as follows:

$$\bar{E}_{ijkl} = 2\bar{G}\delta_{ik}\delta_{jl} + (\bar{K} - \frac{2}{3}\bar{G})\delta_{ij}\delta_{kl} \quad (15)$$

Mortar matrix has distinct behavior in tension and compression. Therefore, in order to adequately characterize the damage in mortar matrix due to tensile and compressive loading, the Cauchy stress tensor (normal and effective) is decomposed into a positive and negative parts using the decomposition technique [Simo and Ju (1987)]. Hereafter, the superscripts “+” and “-” designate, respectively, tensile and compressive entities. Therefor, σ_{ij} and $\bar{\sigma}_{ij}$ can be decomposed as follows:

$$\sigma_{ij} = \sigma_{ij}^+ + \sigma_{ij}^-, \quad \bar{\sigma}_{ij} = \bar{\sigma}_{ij}^+ + \bar{\sigma}_{ij}^- \quad (16)$$

where σ_{ij}^+ is the tensile part and σ_{ij}^- is the compressive part of the stress state. The stress tensors σ_{ij}^+ and σ_{ij}^- can be related to σ_{ij} by

$$\sigma_{ij}^+ = P_{ijkl}^+ \sigma_{kl}, \quad \sigma_{ij}^- = (I_{ijkl} - P_{ijkl}^+) \sigma_{kl} = P_{ijkl}^- \sigma_{kl} \quad (17)$$

such that $P_{ijkl}^+ + P_{ijkl}^- = I_{ijkl}$. The four-order projection tensors P_{ijkl}^+ and P_{ijkl}^- are defined as follows:

$$P_{ijkl}^+ = \sum_{l=1}^3 R(\hat{\sigma}^{(l)}) n_i^{(l)} n_j^{(l)} n_k^{(l)} n_l^{(l)}, \quad P_{ijkl}^- = I_{ijkl} - P_{ijkl}^+ \quad (18)$$

where $R(\hat{\sigma}^{(l)})$ denotes the Heaviside step function computed at l th principle stress $\hat{\sigma}^{(l)}$ of σ_{ij} and $n_i^{(l)}$ is the l th corresponding unit principal direction. In the subsequently development, the superscript hat designates a principal value.

Based on the decomposition in Eq. (16), one can assume that the expression in Eq. (10) to be valid for both tension and compression, however, with decoupled damage evolution in tension and compression such that

$$\sigma_{ij}^+ = M_{ijkl}^+ \bar{\sigma}_{kl}^+, \quad \sigma_{ij}^- = M_{ijkl}^- \bar{\sigma}_{kl}^- \quad (19)$$

where M_{ijkl}^+ is the tensile damage effect tensor and M_{ijkl}^- is the compressive damage effect tensor which can be expressed using Eq. (12) in a decoupled form as a function of tensile and compressive damage variables, φ_{ij}^+ and φ_{ij}^- , respectively, as follows

$$M_{ijkl}^+ = \frac{1}{2} [(\delta_{ij} - \varphi_{ij}^+) \delta_{mn} + \delta_{ij} (\delta_{mn} - \varphi_{mn}^+)] M_{mnkl}^0 \quad (20a)$$

$$M_{ijkl}^- = \frac{1}{2} [(\delta_{ij} - \varphi_{ij}^-) \delta_{mn} + \delta_{ij} (\delta_{mn} - \varphi_{mn}^-)] M_{mnkl}^0 \quad (20b)$$

Now, by substituting Eq. (19) into Eq. (16), one can express the effective stress tensor as the decomposition of the fourth-order damage effect tensor for tension and compression such that

$$\sigma_{ij} = M_{ijkl}^+ \bar{\sigma}_{kl}^+ + M_{ijkl}^- \bar{\sigma}_{kl}^- \quad (21)$$

3.2 Plasticity yield criterion and flow rule

The initial defects not only make the stiffness degradation, but also reduces the strength of material. Therefore, the yield surface should be constructed on the effective (real) stress space. The yield criterion of Lubliner et al. [Lubliner, Oliver, Oller et al. (1989)] that accounts for both tension and compression plasticity is used to describe the plasticity yield surfaces of mortar matrix.

$$f = \sqrt{3\bar{J}_2} + \alpha \bar{I}_1 + \beta (\varepsilon_{eq}^+, \varepsilon_{eq}^-) R(\hat{\sigma}_{max}) \hat{\sigma}_{max} - (1 - \alpha) c^- (\varepsilon_{eq}^-) \leq 0 \quad (22)$$

where $\bar{J}_2 = \frac{1}{2} \bar{s}_{ij} \bar{s}_{ij}$ is the second-invariant of the effective deviatoric stress tensor

$\bar{s}_{ij} = \bar{\sigma}_{ij} - \frac{1}{3} \bar{\sigma}_{kk} \delta_{ij}$, $\bar{I}_1 = \bar{\sigma}_{kk}$ is the first-invariant of the effective Cauchy stress tensor

$\bar{\sigma}_{ij}$, $\hat{\sigma}_{max}$ is the maximum principal effective stress, $R(\hat{\sigma}_{max})$ is the Heaviside step function ($R=1$ for $\hat{\sigma}_{max} > 0$ and $R=0$ for $\hat{\sigma}_{max} < 0$), and the parameters α and β are dimensionless constants which are defined as follows:

$$\alpha = \frac{(f_{b0} / f_0^-) - 1}{2(f_{b0} / f_0^-) - 1}; \quad \beta = (1 - \alpha) \frac{c^- (\varepsilon_{eq}^-)}{c^+ (\varepsilon_{eq}^+)} - (1 + \alpha) \quad (23)$$

where c^- and c^+ are the uniaxial compression and tensile subsequent strength depended on the accumulate equivalent plastic positive strain ε_{eq}^+ and the accumulate equivalent plastic

negative strains ε_{eq}^- respectively, which its expression is as follows [Cicekli, Voyiadjis and Al-Rub (2007); Mura (2013)]:

$$c^- = f_0^- + Q^- (1 - e^{-b^- \varepsilon_{eq}^-}), \quad c^+ = f_0^+ + h^+ \varepsilon_{eq}^+ \quad (24)$$

The accumulate equivalent plastic strain is defined as

$$\varepsilon_{eq}^+ = \int_0^t \dot{\varepsilon}_{eq}^+ dt, \quad \varepsilon_{eq}^- = \int_0^t \dot{\varepsilon}_{eq}^- dt \quad (25)$$

where $\dot{\varepsilon}_{eq}^+, \dot{\varepsilon}_{eq}^-$ is the equivalent plastic strain rate can be defined as

$$\dot{\varepsilon}_{eq}^+ = r(\hat{\sigma}_{ij}) \hat{\varepsilon}_{max}^P, \quad \dot{\varepsilon}_{eq}^- = -(1 - r(\hat{\sigma}_{ij})) \hat{\varepsilon}_{min}^P \quad (26)$$

where $r(\hat{\sigma}_{ij})$ is defined as

$$r(\hat{\sigma}_{ij}) = \frac{\sum_{k=1}^3 \langle \hat{\sigma}_k \rangle}{\sum_{k=1}^3 |\hat{\sigma}_k|} \quad (27)$$

For isotropic linear-elastic material, the fourth-order elasticity tensor \bar{E}_{ijkl} for undamaged material is given by

$$\bar{E}_{ijkl} = 2\bar{G} \delta_{ik} \delta_{jl} + (\bar{K} - \frac{2}{3}\bar{G}) \delta_{ij} \delta_{kl} \quad (28)$$

The plastic potential F^P can be expressed in terms of the Drucker-Prager function as

$$F^P = \sqrt{3J_2} + \alpha^P \bar{I}_1 \quad (29)$$

The evolution of plastic strain tensor can be gained as follows in terms of the above defined plastic potential function

$$d\varepsilon_{ij}^P = d\lambda^P \frac{\partial F^P}{\partial \bar{\sigma}_{ij}} \quad (30)$$

where $d\lambda^P$ is the plastic multiplier, which can be obtained using the standard plasticity consistency condition, $df = 0$, such that

$$f \leq 0, d\lambda^P \geq 0, d\lambda^P f = 0, d\lambda^P df = 0 \quad (31)$$

3.3 The elastic-plastic tangent stiffness in the effective configuration

In order to accelerate convergence, the elasto-plastic tangent stiffness is needed. From Eqs. (22) and (31), one can express the plasticity consistency condition in the effective configuration as follows:

$$df = \frac{\partial f}{\partial \bar{\sigma}_{ij}} d\bar{\sigma}_{ij} + \frac{\partial f}{\partial \hat{\sigma}_{\max}} d\hat{\sigma}_{\max} + \frac{\partial f}{\partial \varepsilon_{eq}^+} d\varepsilon_{eq}^+ + \frac{\partial f}{\partial \varepsilon_{eq}^-} d\varepsilon_{eq}^- = 0 \quad (32)$$

where $d\bar{\sigma}_{ij}$, $d\hat{\sigma}_{\max}$, $d\varepsilon_{eq}^+$, $d\varepsilon_{eq}^-$ can be gained as follow:

$$\begin{aligned} d\bar{\sigma}_{ij} &= \bar{E}_{ijkl} (d\bar{\varepsilon}_{kl} - d\bar{\varepsilon}_{kl}^p) \\ &= 2\bar{G}d\bar{\varepsilon}_{ij} + (\bar{K} - \frac{2}{3}\bar{G})d\bar{\varepsilon}_{kk}\delta_{ij} - d\lambda^p [\sqrt{3}\bar{G} \frac{\bar{s}_{ij}}{\sqrt{J_2}} + 3\bar{K}\alpha^p \delta_{ij}] \end{aligned} \quad (33)$$

$$\begin{aligned} d\hat{\sigma}_{\max} &= n_i^{(1)} d\bar{\sigma}_{ij} n_j^{(1)} = n_i^{(1)} \bar{E}_{ijkl} (d\bar{\varepsilon}_{kl} - d\bar{\varepsilon}_{kl}^p) n_j^{(1)} \\ &= 2\bar{G}n_i^{(1)} d\bar{\varepsilon}_{ij} n_j^{(1)} + (\bar{K} - \frac{2}{3}\bar{G})d\bar{\varepsilon}_{kk} - d\lambda^p [\sqrt{3}\bar{G} \frac{\hat{\sigma}_{\max}}{\sqrt{J_2}} + (3\bar{K}\alpha^p - \bar{G} \frac{\bar{I}_1}{\sqrt{3J_2}})] \end{aligned} \quad (34)$$

$$d\varepsilon_{eq}^+ = r(\hat{\sigma}_{ij}) d\hat{\varepsilon}_{\max}^p = r(\hat{\sigma}_{ij}) n_i^{(1)} \frac{\partial F^p}{\partial \bar{\sigma}_{ij}} n_j^{(1)} d\lambda^p \quad (35)$$

$$d\varepsilon_{eq}^- = -(1 - r(\hat{\sigma}_{ij})) d\hat{\varepsilon}_{\min}^p = -(1 - r(\hat{\sigma}_{ij})) n_i^{(3)} \frac{\partial F^p}{\partial \bar{\sigma}_{ij}} n_j^{(3)} d\lambda^p \quad (36)$$

From the Eq. (32), $d\lambda^p$ can be solves as

$$d\lambda^p = \frac{Qd\bar{\varepsilon}}{H} \quad (37)$$

where Q and H are given as

$$Q = 2\bar{G} \frac{\partial f}{\partial \bar{\sigma}_{kl}} + (\bar{K} - \frac{2}{3}\bar{G}) \frac{\partial f}{\partial \bar{\sigma}_{ij}} \delta_{kl} \delta_{ij} + 2\bar{G} \frac{\partial f}{\partial \hat{\sigma}_{\max}} n_k^{(1)} n_l^{(1)} + (\bar{K} - \frac{2}{3}\bar{G}) \frac{\partial f}{\partial \hat{\sigma}_{\max}} \delta_{kl} \quad (38)$$

$$\begin{aligned} H &= 3\bar{G} + 9\bar{K}\alpha^p \alpha + \beta R(\hat{\sigma}_{\max}) (\sqrt{3}\bar{G} \frac{\hat{\sigma}_{\max}}{\sqrt{J_2}} + 3\bar{K}\alpha^p - \frac{\bar{G}\bar{I}_1}{\sqrt{3J_2}}) \\ &+ (1-r) \frac{\partial f}{\partial \varepsilon_{eq}^-} \frac{\partial F^p}{\partial \hat{\sigma}_{\min}} - r \frac{\partial f}{\partial \varepsilon_{eq}^+} \frac{\partial F^p}{\partial \hat{\sigma}_{\max}} \end{aligned} \quad (39)$$

where $\frac{\partial f}{\partial \varepsilon_{eq}^+}$, $\frac{\partial f}{\partial \varepsilon_{eq}^-}$ and $\frac{\partial F^p}{\partial \bar{\sigma}_{ij}}$ can be derived from expression (22) (29) as

$$\frac{\partial f}{\partial \varepsilon_{eq}^+} = -\left\langle \hat{\sigma}_{\max} \right\rangle \frac{c^-(1-\alpha)h^+}{(c^+)^2}, \quad \frac{\partial f}{\partial \varepsilon_{eq}^-} = -(1-\alpha)[Q^-b^-e^{-b^-\varepsilon_{eq}^-}] \quad (40)$$

$$\frac{\partial F^P}{\partial \bar{\sigma}_{ij}} = \frac{3}{2} \frac{\bar{s}_{ij}}{\sqrt{3J_2}} + \alpha^P \delta_{ij} \quad (41)$$

Then, by substituting expression (37) into $d\bar{\sigma}_{ij} = \bar{E}_{ijkl}(d\bar{\varepsilon}_{kl} - d\lambda^P \frac{\partial F^P}{\partial \bar{\sigma}_{kl}})$, the stress rate

$d\bar{\sigma}_{ij}$ can be rewritten as a function of the rate of the strain $d\bar{\varepsilon}_{kl}$ as follows:

$$d\bar{\sigma}_{ij} = \left(\bar{E}_{ijkl} - \frac{\bar{E}_{ijmn} Q_{kl} \frac{\partial F^P}{\partial \bar{\sigma}_{mn}}}{H} \right) d\bar{\varepsilon}_{kl} = \bar{E}_{ijkl}^t d\bar{\varepsilon}_{kl} \quad (42)$$

where \bar{E}^t is the elasto-plastic tangent stiffness for undamaged mortar phase.

3.4 Tensile and compressive damage surfaces

The following damage growth function which is proposed by Chow et al. [Chow and Wang (1987)] and used by many others [Al-Rub and Voyiadjis (2006); Voyiadjis, Al-Rub and Palazotto (2003); Voyiadjis, Al-Rub and Palazotto (2004); Mazars and Pijaudier-Cabot (1989)] is adopted in this study. However, this function is generalized in Cicekli et al. [Cicekli, Voyiadjis and Al-Rub (2007)] in order to incorporate both tensile and compressive damage separately, such that

$$g^\pm = \sqrt{\frac{1}{2} Y_{ij}^\pm L_{ijkl}^\pm Y_{kl}^\pm} - K^\pm(\varphi_{eq}^\pm) \leq 0 \quad (43)$$

where Y_{ij}^\pm is the damage driving force which can be explained as the energy release rate, K^\pm is the tensile or compressive damage isotropic softening function such that $K^\pm = K_0^\pm$ when there is no damage, where K_0^\pm is the tensile or compressive initial damage parameter (i.e. damage threshold), and L_{ijkl}^\pm is a fourth-order symmetric tensor and is presented in matrix form as follows

$$L_{ijkl}^\pm = \begin{bmatrix} 1 & \mu^\pm & \mu^\pm & 0 & 0 & 0 \\ \mu^\pm & 1 & \mu^\pm & 0 & 0 & 0 \\ \mu^\pm & \mu^\pm & 1 & 0 & 0 & 0 \\ 0 & 0 & 0 & 2(1-\mu^\pm) & 0 & 0 \\ 0 & 0 & 0 & 0 & 2(1-\mu^\pm) & 0 \\ 0 & 0 & 0 & 0 & 0 & 2(1-\mu^\pm) \end{bmatrix} \quad (44)$$

where μ^\pm is a material constant satisfying $-1/2 \leq \mu^\pm \leq 1$. The damage driving force can be derived by the thermodynamic laws and the expression of elastic free energy as follows [Cicekli, Voyiadjis and Al-Rub (2007)]:

$$Y_{rs}^\pm = -\frac{1}{2} \bar{E}_{ijmn}^{-1} \bar{\sigma}_{mn} \frac{\partial M_{ijpq}}{\partial \varphi_{rs}^\pm} \bar{\sigma}_{pq} \quad (45)$$

where $\frac{\partial M_{ijpq}}{\partial \varphi_{rs}^\pm}$ can be derived as follows:

$$\frac{\partial M_{ijpq}^\pm}{\partial \varphi_{rs}^\pm} = \frac{\partial (M_{ijab}^{\pm} M_{abpq}^0)}{\partial \varphi_{rs}^\pm} = \frac{\partial M_{ijab}^{\pm}}{\partial \varphi_{rs}^\pm} M_{abpq}^0 = -J_{ijabrs} M_{abpq}^0 \quad (46)$$

in which J_{ijpqrs} is a sixth-order tensor and is given by Lubliner et al. [Lubliner, Oliver, Oller et al. (1989)]

$$J_{ijpqrs} = \frac{1}{2} (\delta_{pq} \delta_{ir} \delta_{js} + \delta_{ij} \delta_{pr} \delta_{qs}) \quad (47)$$

And φ_{eq}^\pm is the accumulate equivalent damage which can be defined as follows:

$$\varphi_{eq}^\pm = \int_0^t \dot{\varphi}_{eq}^\pm dt \quad \text{with} \quad \dot{\varphi}_{eq}^\pm = \sqrt{\dot{\varphi}_{ij}^\pm \dot{\varphi}_{ij}^\pm} \quad (48)$$

where the evolution equation for damage tensor φ_{ij} is defined as follows:

$$d\varphi_{ij}^\pm = d\lambda_d^\pm \frac{\partial g^\pm}{\partial Y_{ij}^\pm} \quad (49)$$

where $d\lambda_d^\pm$ is the damage multiplier which can be obtained from the following damage consistency conditions

$$g^\pm \leq 0, d\lambda_d^\pm \geq 0, d\lambda_d^\pm g^\pm = 0, d\lambda_d^\pm dg^\pm = 0 \quad (50)$$

The following tensile and compressive damage evolution laws proposed by Kim [Mura (2013)] are used to model the damage development of mortar due to its better predictions than the exponential damage laws [Mazars and Pijaudier-Cabot (1989)], such that

$$\begin{cases} \varphi_{eq}^+ = B^+ \left(\frac{K_0^+}{K^+} \right) \left(\frac{K^+}{K_0^+} - 1 \right)^{q^+} \\ \varphi_{eq}^- = B^- \left(\frac{K^-}{K_0^-} - 1 \right)^{q^-} \end{cases} \quad (51)$$

where B^\pm and q^\pm are material constants. Furthermore, the damage isotropic softening functions can be obtained as follows by taking the time derivative of the above Eq. (51)

$$\begin{cases} \dot{K}^+ = \frac{K^+}{B^+(q^+K_0^+ - 1 + \frac{K_0^+}{K^+})} \left(\frac{K^+}{K_0^+} - 1 \right)^{1-q^+} \dot{\varphi}_{eq}^+ \\ \dot{K}^- = \frac{K_0^-}{B^-q^-} \left(\frac{K^-}{K_0^-} - 1 \right)^{1-q^-} \dot{\varphi}_{eq}^- \end{cases} \quad (52)$$

Therefore, the partial derivation of the damage softening function K^\pm to the accumulate equivalent damage φ_{ij}^\pm can be written as follows:

$$\frac{\partial K^\pm}{\partial \varphi_{eq}^\pm} = \frac{K_0^\pm}{B^\pm q^\pm} \left(\frac{B^\pm}{\varphi_{eq}^\pm} \right)^{\frac{q^\pm-1}{q^\pm}} \quad (53)$$

According to the damage consistency conditions (50) and the tensile-compressive damage surfaces (43), the increment of the damage function can be written as follows:

$$dg^\pm = \frac{\partial g^\pm}{\partial Y_{ij}^\pm} dY_{ij}^\pm + \frac{\partial g^\pm}{\partial K^\pm} dK^\pm = 0 \quad (54)$$

However, since the damage driving force Y_{ij}^\pm is a function of stress σ_{ij}^\pm and damage φ_{ij}^\pm , one can write the following:

$$dY_{ij}^\pm = \frac{\partial Y_{ij}^\pm}{\partial \sigma_{kl}^\pm} d\sigma_{kl}^\pm + \frac{\partial Y_{ij}^\pm}{\partial \varphi_{kl}^\pm} d\varphi_{kl}^\pm \quad (55)$$

And $d\sigma_{kl}^\pm$ can be obtained from Eqs. (10) and (12) as follows:

$$d\sigma_{kl}^\pm = \frac{\partial M_{klrs}^\pm}{\partial \varphi_{mn}^\pm} d\varphi_{mn}^\pm \bar{\sigma}_{rs}^\pm + M_{klrs}^\pm d\bar{\sigma}_{rs}^\pm \quad (56)$$

By substituting Eqs. (49), (55) and (56) into Eq. (54), one can obtain the following relation

$$\begin{aligned} dg^\pm &= \frac{\partial g^\pm}{\partial Y_{ij}^\pm} \frac{\partial Y_{ij}^\pm}{\partial \sigma_{kl}^\pm} \frac{\partial M_{klrs}^\pm}{\partial \varphi_{mn}^\pm} \bar{\sigma}_{rs}^\pm \frac{\partial g^\pm}{\partial Y_{mn}^\pm} d\lambda_d^\pm + \frac{\partial g^\pm}{\partial Y_{ij}^\pm} \frac{\partial Y_{ij}^\pm}{\partial \sigma_{kl}^\pm} M_{klrs}^\pm d\bar{\sigma}_{rs}^\pm \\ &+ \frac{\partial g^\pm}{\partial Y_{ij}^\pm} \frac{\partial Y_{ij}^\pm}{\partial \varphi_{kl}^\pm} \frac{\partial g^\pm}{\partial Y_{kl}^\pm} d\lambda_d^\pm + \frac{\partial g^\pm}{\partial K^\pm} \frac{\partial K^\pm}{\partial \varphi_{eq}^\pm} d\lambda_d^\pm = 0 \end{aligned} \quad (57)$$

And the damage multiplier $d\lambda_d^\pm$ can be solved as follows:

$$d\lambda_a^\pm = - \frac{\frac{\partial g^\pm}{\partial Y_{ij}^\pm} \frac{\partial Y_{ij}^\pm}{\partial \sigma_{kl}^\pm} M_{klmn}^\pm d\bar{\sigma}_{mn}^\pm}{\frac{\partial g^\pm}{\partial Y_{ij}^\pm} \frac{\partial Y_{ij}^\pm}{\partial \sigma_{kl}^\pm} \frac{\partial M_{klrs}^\pm}{\partial \varphi_{mn}^\pm} \bar{\sigma}_{rs}^\pm \frac{\partial g^\pm}{\partial Y_{mn}^\pm} + \frac{\partial g^\pm}{\partial Y_{ij}^\pm} \frac{\partial Y_{ij}^\pm}{\partial \varphi_{kl}^\pm} \frac{\partial g^\pm}{\partial Y_{kl}^\pm} + \frac{\partial g^\pm}{\partial K^\pm} \frac{\partial K^\pm}{\partial \varphi_{eq}^\pm}} \quad (58)$$

where $\frac{\partial g^\pm}{\partial K^\pm} = -1$, $\frac{\partial g^\pm}{\partial Y_{ij}^\pm} = \frac{L_{ijkl}^\pm Y_{kl}^\pm}{\sqrt{2Y_{ij}^\pm L_{ijkl}^\pm Y_{kl}^\pm}}$, $\frac{\partial Y_{ij}^\pm}{\partial \sigma_{kl}^\pm} = (M_{mnpq}^\pm)^{-1} J_{mnpqij} \epsilon_{kl}^{\pm e}$.

4 The FEM for concrete specimen on meso scale

4.1 Cohesive element for ITZ

The cohesive element with three pairs of nodes as presented in Fig. 4 is used to model the mechanical response of ITZ contained in concrete. For any point P in cohesive element, its relative displacement $[\mathbf{u}'_P]$ can be given as

$$[\mathbf{u}'_P] = \mathbf{N}_{coh} \mathbf{T}_\alpha \mathbf{u}_{coh}^e \quad (59)$$

where \mathbf{T}_α is the coordinate transformation matrix, $\mathbf{u}_{coh}^e = \{\mathbf{u}_1 \ \mathbf{u}_2 \ \mathbf{u}_3 \ \mathbf{u}_{1'} \ \mathbf{u}_{2'} \ \mathbf{u}_{3'}\}^T$ is the displacement vector of cohesive element, $\mathbf{N}_{coh} = \{\mathbf{N}_1 \ \mathbf{N}_2 \ \mathbf{N}_3 \ \mathbf{N}_{1'} \ \mathbf{N}_{2'} \ \mathbf{N}_{3'}\}^T$ is the shape function matrix of cohesive element, \mathbf{N}_i is the shape function matrix at i node of tetrahedron element, which for i' node corresponding to i node, its shape function can be defined as $\mathbf{N}_{i'} = -\mathbf{N}_i$.

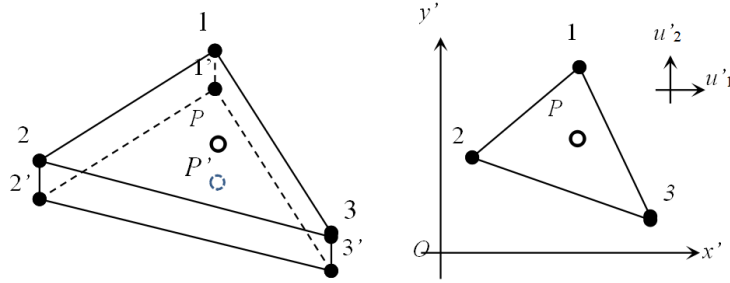


Figure 4: Cohesive element with three pairs of nodes

4.2 Governing equations

The governing equations for concrete specimen at the meso-scale are given as

$$\begin{cases} \nabla \cdot \boldsymbol{\sigma} + \mathbf{b} = 0 & \text{in } \Omega \\ \mathbf{u} = \bar{\mathbf{u}} & \text{on } \Gamma_u^\tau \\ \boldsymbol{\sigma} \cdot \mathbf{n}_f = \bar{\mathbf{f}} & \text{on } \Gamma_f^\tau \\ \boldsymbol{\sigma} \cdot \mathbf{n}_{coh} = \mathbf{t}_{coh} & \text{on } \Gamma_{coh}^\tau \end{cases} \quad (60)$$

where \mathbf{b} is the body force. Ω denotes the computational domain. Γ_u^τ denotes the displacement boundary at τ time. Γ_f^τ denotes the force boundary at τ time, Γ_{coh}^τ denotes the boundary of material at τ time, ∇ is the gradient operator, \mathbf{n}_f is the normal of the force boundary Γ_f^τ , \mathbf{n}_{coh} is the normal of ITZ surface Γ_{coh}^τ . All of the boundary condition is presented in Fig. 5.

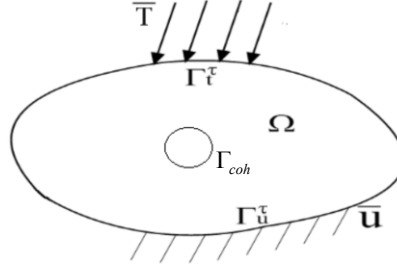


Figure 5: Concrete domain with inclusion

4.3 The weak form of governing equations

The weak form of the equilibrium equation can be given as

$$\delta W = \delta W_{ext} + \delta W_{coh} + \delta W_{int} = 0 \quad (61)$$

With

$$\delta W_{int} = \int_{\Omega} \delta \nabla_s \mathbf{u}^T : \mathbf{E}^t : \nabla_s \mathbf{u} dV \quad (62)$$

$$\delta W_{ext} = - \int_{\Omega} \delta \mathbf{u} \cdot \mathbf{b} d\Omega - \int_{\Gamma_f^\tau} \delta \mathbf{u} \cdot \bar{\mathbf{f}} d\Gamma \quad (63)$$

$$\delta W_{coh} = \int_{\Gamma_{coh}^\tau} \delta [\mathbf{u}'] \mathbf{t}_{coh} d\Gamma \quad (64)$$

where ∇_s is the symmetric gradient operator, \mathbf{u} and $\delta \mathbf{u}$ are the trial and test function which should lie in the following spaces

$$U = \{ \mathbf{u} \mid \mathbf{u} \in C^0, \mathbf{u} = \bar{\mathbf{u}} \text{ on } \Gamma_u^\tau, \mathbf{u} \text{ discontinuous on } \Gamma_{coh}^\tau \} \quad (65)$$

$$U_0 = \{ \delta \mathbf{u} \mid \delta \mathbf{u} \in C^0, \delta \mathbf{u} = 0 \text{ on } \Gamma_u^\tau, \delta \mathbf{u} \text{ discontinuous on } \Gamma_{coh}^\tau \} \quad (66)$$

And $[\mathbf{u}']$ is the relative displacement of ITZ in local coordination, which can be obtain as formula (59). \mathbf{E}^t is the elasto-plastic-damage matrix.

The rates of the virtual works in Eqs. (62)-(64) can be given as

$$\delta \dot{W}_{int} = \int_{\Omega} \delta \nabla_s \mathbf{u}^T : \mathbf{E}^t : \nabla_s \dot{\mathbf{u}} dV \quad (67)$$

$$\delta \dot{W}_{ext} = - \int_{\Omega} \delta \mathbf{u} \cdot \dot{\mathbf{b}} d\Omega - \int_{\Gamma_f^\tau} \delta \mathbf{u} \cdot \dot{\bar{\mathbf{f}}} d\Gamma \quad (68)$$

$$\delta\dot{W}_{coh} = \int_{\Gamma_{coh}^{\tau}} \delta[\mathbf{u}'] \dot{\mathbf{t}}_{coh} d\Gamma \quad (69)$$

4.4 The domain discretization

According to the rates equation of the virtual works $\delta\dot{W} = 0$, the domain of concrete with inclusions can be discretized as follows

$$\sum_{e=1}^{N_e} \left(\int_{\Omega^e} (\delta \nabla_s \mathbf{u}^T : \mathbf{E}^t : \nabla_s \dot{\mathbf{u}} - \delta \dot{\mathbf{u}} \cdot \dot{\mathbf{b}}) d\Omega - \int_{\Gamma_f^e} \delta \mathbf{u} \cdot \dot{\mathbf{f}} d\Gamma \right) - \sum_{e=1}^{N_{e'}} \left(\int_{\Gamma_{coh}^e} \delta[\mathbf{u}'] \mathbf{D}_{coh} [\dot{\mathbf{u}}'] d\Gamma \right) = 0 \quad (70)$$

where N_e is the number of solid element. $N_{e'}$ is the number of cohesive element. Substitute the formula (59) into the Eq. (69), the discretization equation can be rewritten as

$$\begin{aligned} & \sum_{e=1}^{N_e} \delta(\mathbf{u}^e)^T \int_{\Omega^e} (\mathbf{B}^T \mathbf{E}^t \mathbf{B} \dot{\mathbf{u}}^e - \mathbf{N}^T \dot{\mathbf{b}}) d\Omega - \sum_{e=1}^{N_{e'}} \delta(\mathbf{u}^e)^T \int_{\Gamma_t^e} \mathbf{N}^T \dot{\mathbf{f}} d\Gamma \\ & - \sum_{e=1}^{N_{e'}} \delta(\mathbf{u}_{coh}^e)^T \int_{\Gamma_{coh}^e} \mathbf{N}_{coh}^T \mathbf{T}_\alpha^T \mathbf{D}_{coh} \mathbf{T}_\alpha \mathbf{N}_{coh} d\Gamma \dot{\mathbf{u}}_{coh}^e = 0 \end{aligned} \quad (71)$$

$$\text{Let } \mathbf{K}_s^e = \int_{\Omega^e} \mathbf{B}^T \mathbf{E}^t \mathbf{B} d\Omega, \quad \mathbf{K}_{coh}^e = \int_{\Gamma_{coh}^e} \mathbf{N}_{coh}^T \mathbf{T}_\alpha^T \mathbf{D}_{coh} \mathbf{T}_\alpha \mathbf{N}_{coh} d\Gamma, \quad \dot{\mathbf{f}}_t^e = \int_{\Gamma_t^e} \mathbf{N}^T \dot{\mathbf{f}} d\Gamma,$$

$\dot{\mathbf{f}}_b^e = \int_{\Omega^e} \mathbf{N}^T \dot{\mathbf{b}} d\Omega$. Introduce the choose matrix \mathbf{C}_e , and let $\mathbf{C}_e^{coh} = [\mathbf{C}_e^{(1)} \quad \mathbf{C}_e^{(2)}]^T$, then the node displacement vector in element can be given as

$$\dot{\mathbf{u}}^e = \mathbf{C}_e \dot{\mathbf{U}}, \quad \dot{\mathbf{u}}_{coh}^e = \mathbf{C}_e^{coh} \dot{\mathbf{U}} \quad (72)$$

where $\dot{\mathbf{U}}$ is the node displacement increment in whole domain. So, the Eq. (71) is rewritten as

$$\delta \mathbf{U}^T \left[\sum_{e=1}^{N_e} \mathbf{C}_e^T \mathbf{K}_s^e \mathbf{C}_e \dot{\mathbf{U}} - \sum_{e=1}^{N_{eb}} \mathbf{C}_e^T \dot{\mathbf{f}}_b^e - \sum_{e=1}^{N_{et}} \mathbf{C}_e^T \dot{\mathbf{f}}_t^e \right] + \delta \mathbf{U}^T \sum_{e=1}^{N_{e'}} \mathbf{C}_e^{cohT} \mathbf{K}_{coh}^e \mathbf{C}_e^{coh} \dot{\mathbf{U}} = 0 \quad (73)$$

$$\text{Let } \mathbf{K}_s = \sum_e \mathbf{C}_e^T \mathbf{K}_s^e \mathbf{C}_e, \quad \mathbf{K}_{coh} = \sum_e \mathbf{C}_e^{cohT} \mathbf{K}_{coh}^e \mathbf{C}_e^{coh}, \quad \dot{\mathbf{f}}^{ext} = \sum_{e=1}^{N_{eb}} \mathbf{C}_e^T \dot{\mathbf{f}}_b^e + \sum_{e=1}^{N_{et}} \mathbf{C}_e^T \dot{\mathbf{f}}_t^e.$$

Therefore, the weak form (73) of discretization equation can be further rewritten as

$$\delta \dot{W} = \delta \mathbf{U}^T (\mathbf{K}_s + \mathbf{K}_{coh}) \dot{\mathbf{U}} - \delta \mathbf{U}^T \dot{\mathbf{f}}^{ext} = 0 \quad (74)$$

Since $\delta \mathbf{U}$ is arbitrary, the global stiffness equation for increment format is obtained as follows from Eq. (74)

$$(\mathbf{K}_s + \mathbf{K}_{coh}) \dot{\mathbf{U}} = \dot{\mathbf{f}}^{ext} = \dot{\mathbf{f}}^{ext} - \dot{\mathbf{f}}^{in} \quad (75)$$

$$\text{where } \dot{\mathbf{f}}^{ext} = \sum_e \int_{\Omega^e} \mathbf{N}^T \mathbf{b} d\Omega + \sum_e \int_{\Gamma_t^e} \mathbf{N}^T \dot{\mathbf{f}} d\Gamma,$$

$$\dot{\mathbf{f}}^{in} = \sum_e \int_{\Omega^e} \mathbf{B}^T \boldsymbol{\sigma} d\Omega + \sum_e \int_{\Gamma_{coh}^e} \mathbf{N}_{coh}^T \mathbf{T}_\alpha^T \mathbf{t}_{coh} d\Gamma.$$

4.5 The generation of the meso-mesh based on the FEM for concrete specimen

Assuming the aggregates' shape are all sphere or ellipsoid, given the aggregate volume fraction with different gradations, the number of them can be obtained by the gradation theory of concrete. Then, one can random throw particles from bigger to smaller into the domain of specimen by Monte Carlo method under the condition of no overlap each other. Based on the random particles geometric model, the particle groups are discretized from big to small gradation by tetrahedron gradually mesh generation method in which the grid is density at the edges of particles while sparse far away from the edges as shown in Fig. 6(b), and then the mortar matrix is meshed with the same density grid at the edge of particle. Finally, the cohesive elements are embedded into the interfaces between aggregates and mortar matrix as shown in Fig. 6(c).

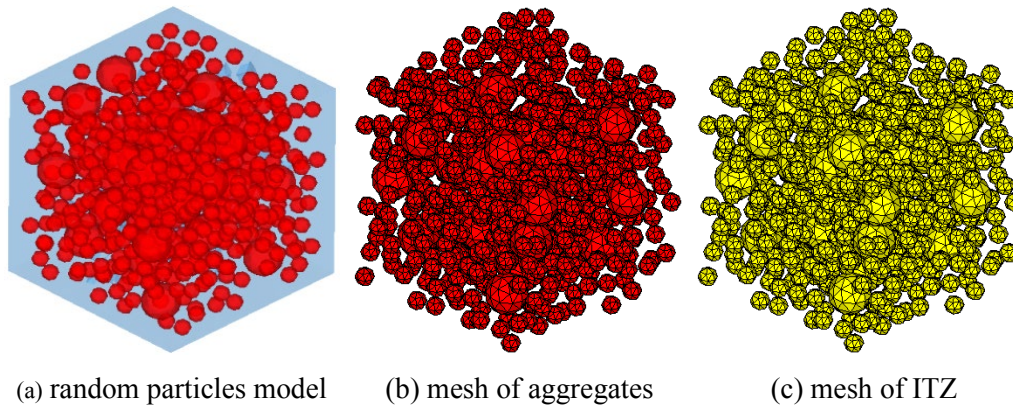


Figure 6: Concrete cube sample

5 Verification of modeling

In order to verify the effectiveness of the proposed FEM model for concrete in meso scale. The uniaxial tension and compression numerical experiments of concrete sample with size of 150 mm×150 mm×150 mm is implemented. The modulus and Poisson's ratio of aggregate are 52,000 MPa and 0.18 respectively. And the modulus and Poisson's ratio of mortar matrix are 26,000 MPa and 0.2 respectively. For the other two material components, their material parameters involved are presented in Tab. 1 and Tab. 2. And the aggregate volume fractions are 29.3% with grain size of 30 mm and 20.7% with grain size of 15 mm respectively. The whole failure process for uniaxial tension and compression of concrete sample under the displacement loading control are shown in Fig. 7 and Fig. 8 respectively. From the two figures, the failures are taken on in the tearing mode of interlaminar during tension, while in the shear fracturing mode of 'X' type with striping on sample edge during compression, which are good agree with that of experiment as shown in Fig. 9 [Yan (2006)]. Their ultimate interface damage status are presented in Fig. 10 and Fig. 11.

Table 1: Material properties of mortar matrix used in the analysis

	Tensile material constants					Yield criteria		Compressive material constants					
	f_0^+ (MPa)	K_0^+ (MPa)	h^+ (MPa)	B^+	q^+	α	α^p	f_0^- (MPa)	Q^- (MPa)	b^-	K_0^- (MPa)	B^-	q^-
Mortar	3.0	3.0	10,000	1.3	1.1	0.12	0.2	15	80	820	20	0.15	1.4

Table 2: Material properties of ITZ used in the analysis

	K_n^0 (MPa/mm)	K_s^0 (MPa/mm)	σ_n^0 (MPa)	τ_s^0 (MPa)	τ_t^0 (MPa)	G_f^I (N/mm)	G_f^{II} (N/mm)
ITZ	5×10^8	5×10^8	2.0	4.0	4.0	0.02	0.04

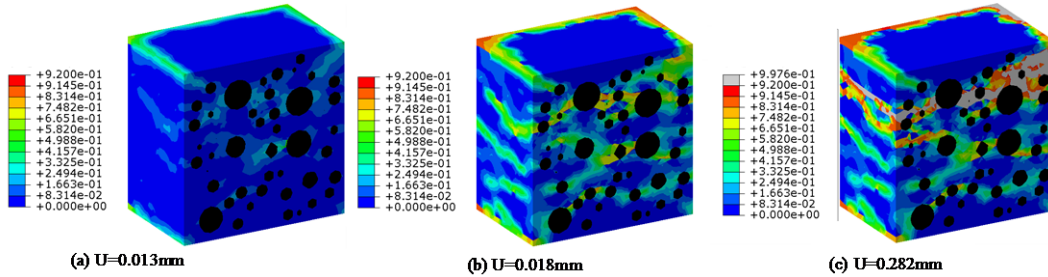


Figure 7: The equivalent tensile damage distribution for uniaxial tension

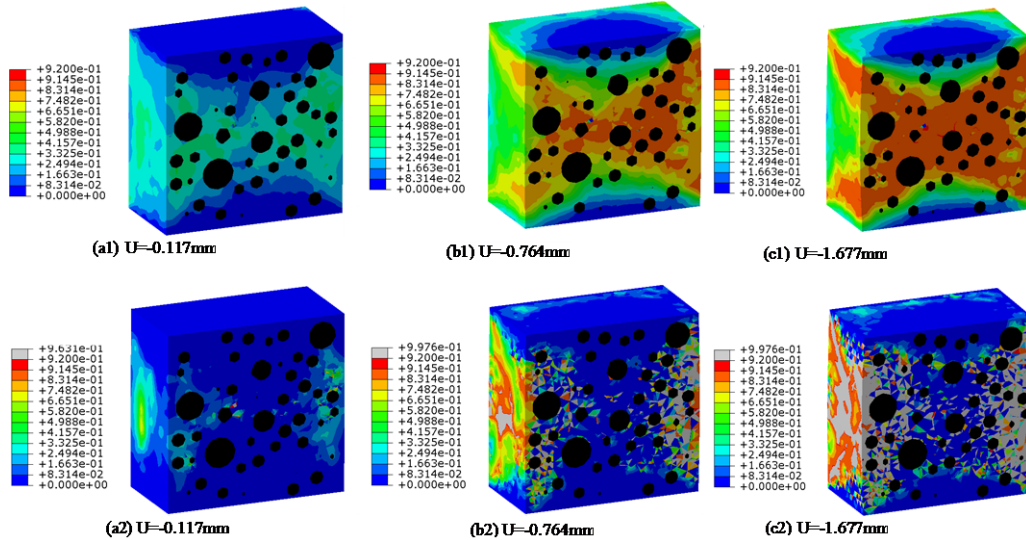


Figure 8: The equivalent damage evolution for uniaxial compression (a1, b1 and c1 for equivalent tensile damage; a2, b2 and c2 for equivalent compressive damage)



Figure 9: The failure mode under uniaxial compression for concrete sample

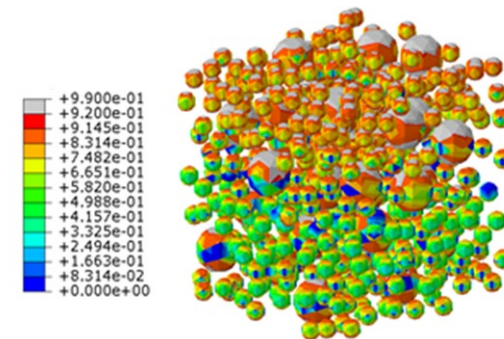


Figure 10: Interface damage distribution for tension

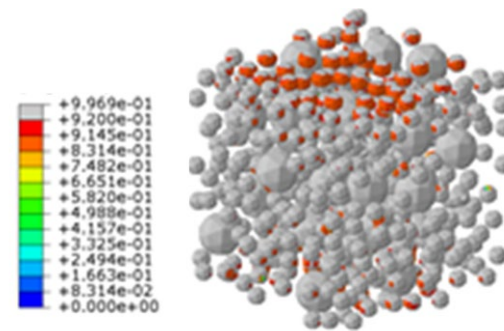


Figure 11: Interface damage distribution for compression

Through averaging of the axial stress on these element integration points, the uniaxial stress-strain curve is obtained as shown in Fig. 12, which keeps a good trend to that of experiment [Wischers (1978)] except on the residual stage. What causes the difference at the residual stage is that the present model does not consider the complicated aggregate shape. When the irregular aggregates take on some sharper corners, the local stress concentrate effect will be more remarkable so that the residual strength at ITZ become weaker. Therefore, the effectiveness of the proposed concrete micro FEM embedded a large number of cohesive elements in ITZ has been verified.

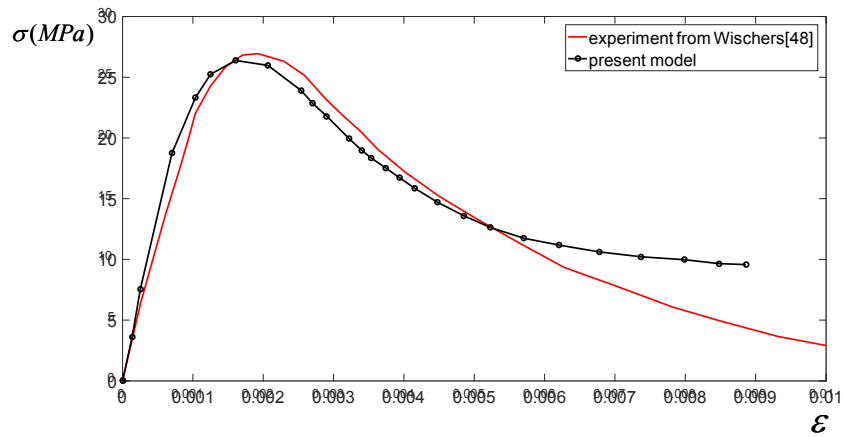


Figure 12: The stress-strain curve of uniaxial compression for concrete material

6 The effect of initial defects on the overall properties of concrete

6.1 The effect of initial micro holes

In order to investigate the effect of initial micro voids on the overall properties of concrete material, the concrete samples with different porosity (0.2%, 0.5%, 1.0%, 1.5%, 2.0%) are employed, and their failure process under the action of uniaxial tension and uniaxial compression are simulated by the proposed model. From the calculated stress field and the applied displacement loading, the uniaxial stress-strain curves have been extracted, as shown in Fig. 13 and Fig. 14. From the obtained stress-strain relationship, it can be obtained that both the peak value and the energy release rate decrease with the increase of porosity. That is to say, the more initial micro voids in concrete, the lower its strength and the more brittle the material is, whether under tension or compression. It is emphasized that the compression characteristic is different from that of air-entrained concrete due to the resisting effect of the internal air press in voids.

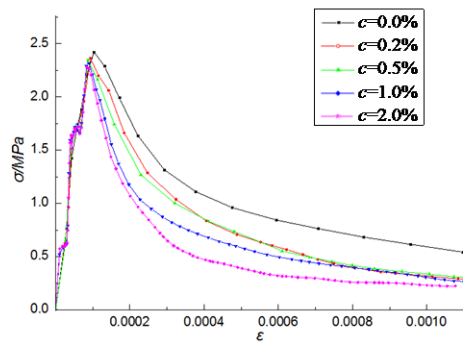


Figure 13: The tensile stress-strain curve with different porosity

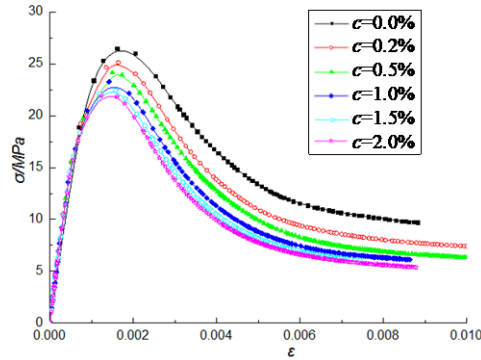


Figure 14: The compressive stress-strain curve with different porosity

6.2 The effect of ITZ characteristics

To better capture the failure mode and fracturing path, the 2-D model in meso scale is employed with the proposed constitutive laws of ITZ and mortar matrix. To explore the effect of ITZ characteristics on the overall properties of concrete, the concrete specimens with different ITZ stiffness and strength are chosen. Specifically, under the condition of same porosity 0.5%, same aggregate volume fraction and same fracture energy 0.03 N/mm, two case of ITZ stiffness are chosen as in Tab. 3, and other two case of ITZ strength are chosen as in Tab. 4. The other parameters refer to the Tab. 1 and Tab. 2.

Table 3: ITZ stiffness of two case

	Grain type	Normal stiffness K_n^0 (MPa/mm)	Shear stiffness K_s^0 (MPa/mm)
Case I	ITZ for big grain	2.8×10^5	2.0×10^5
	ITZ for small grain	1.4×10^5	1.0×10^5
Case II	ITZ for big grain	1.4×10^5	1.0×10^5
	ITZ for small grain	1.4×10^5	1.0×10^5

The obtained damage distribution and evolution for different ITZ stiffness are presented as Fig. 15 and Fig. 16, which show that the stiffness of ITZ can directly influence the strength and the damage distribution of concrete sample. When the stiffness of ITZ for big aggregate group is larger than that of small one, the stress concentration effect at big grain boundary is less than that at small one. The main reason is that the ITZ attached on small aggregate bears more deformation due to the larger stiffness of the ITZ attached on large aggregate under the same displacement load. When the specimen is in tensile stress status, the large particles takes on an inhibitory effects on the small one which causes the different damage development path shown in Fig. 15. When the specimen is in compressive-shear stress status, the large aggregate takes on a shield effect on small one as shown in Fig. 16.

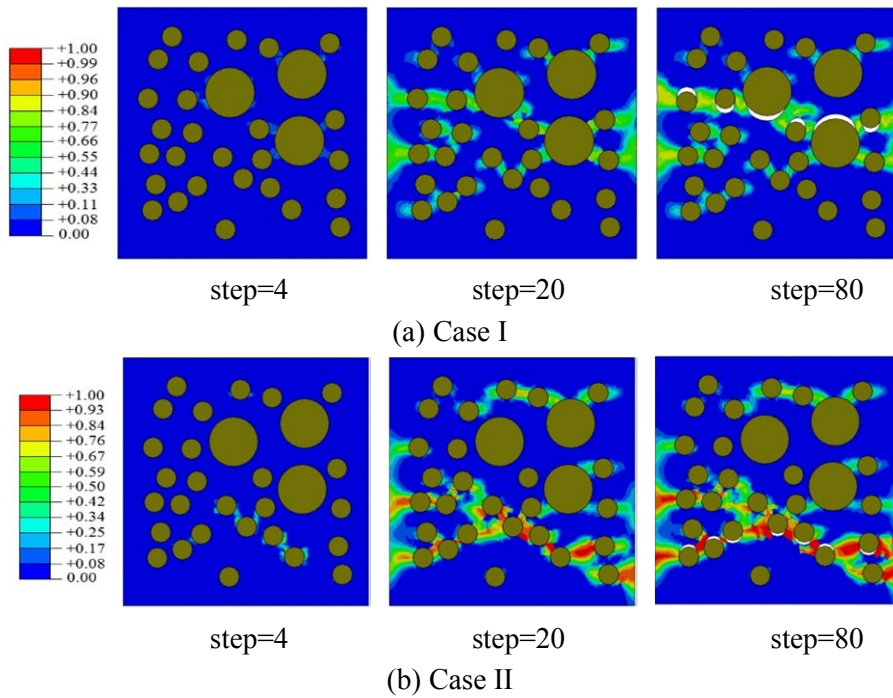


Figure 15: The equivalent positive damage distribution for uniaxial tension (different stiffness)

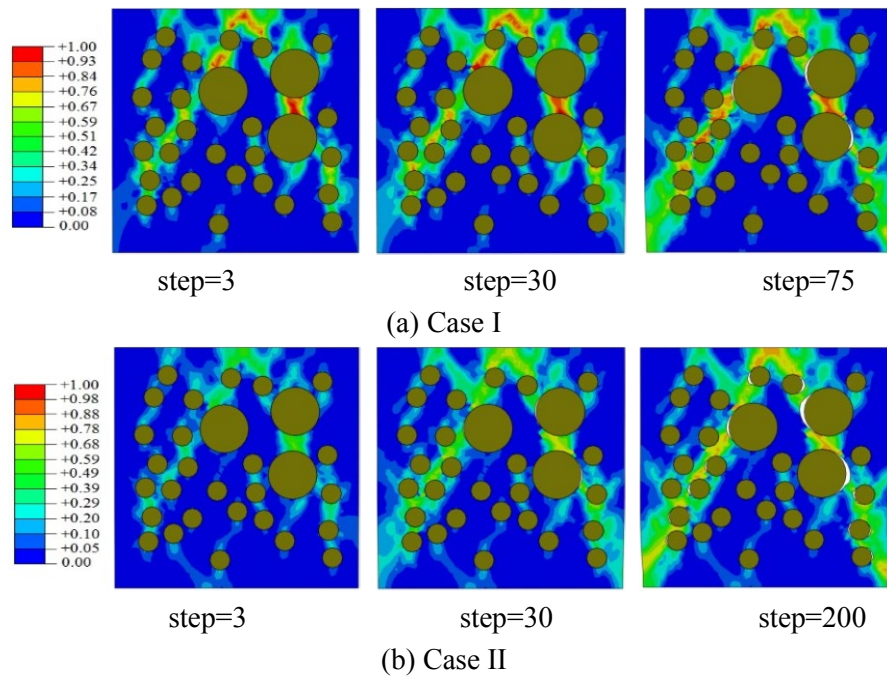


Figure 16: The equivalent positive damage distribution for uniaxial compression (different stiffness)

The same process as the above, the obtained damage distribution and evolution for different ITZ strength are presented in Fig. 17 and Fig. 18. When the normal strength of ITZ is less than the tension strength of mortar matrix, the damages firstly produce in ITZ, and develop to the mortar area from the grain boundary as shown in Fig. 17(a). However, when the normal strength of ITZ is selected to the same of tension strength of mortar matrix, the damages in mortar matrix always develop prior to ITZ due to its compared softer stiffness as presented in Fig. 17(b). What's more, the damage strip is more concentrate in mortar matrix for the case of higher ITZ strength. For the compressive-shear stress status, the damage evolution path is almost same as presented in Fig. 18 for the two case due to both of the shear strength of ITZ not reaching that of mortar matrix.

Table 4: ITZ strength of two case

	Normal strength σ_n^0 (MPa)	Shear strength τ_s^0 (MPa)
Case I	2.0	2.0
Case II	3.0	3.0

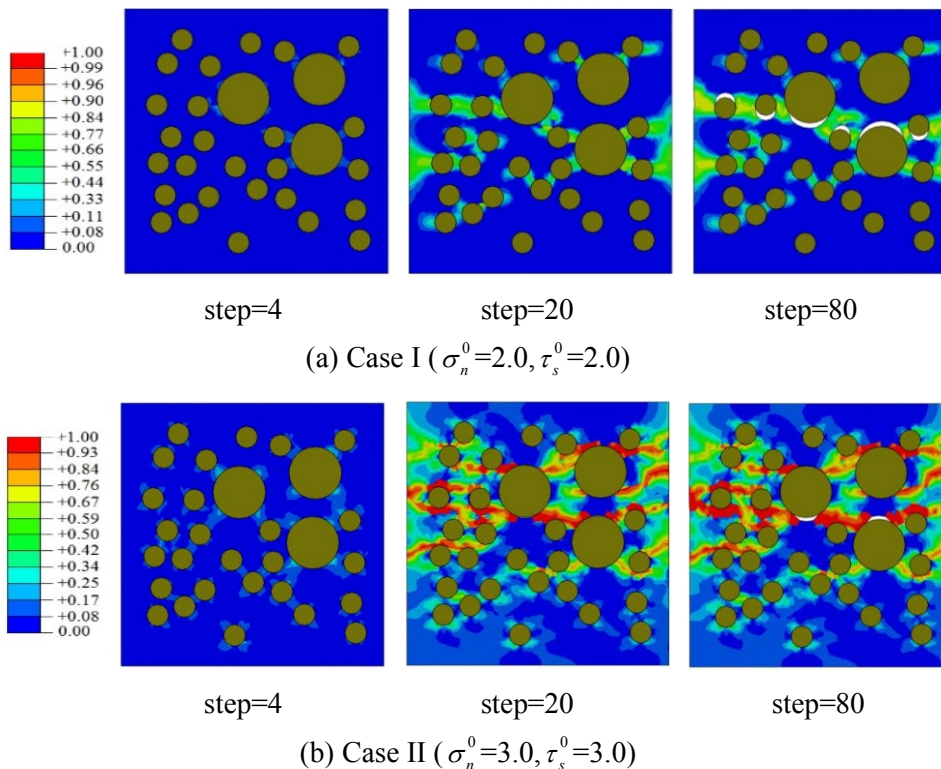


Figure 17: The equivalent positive damage distribution for uniaxial tension (different strength)

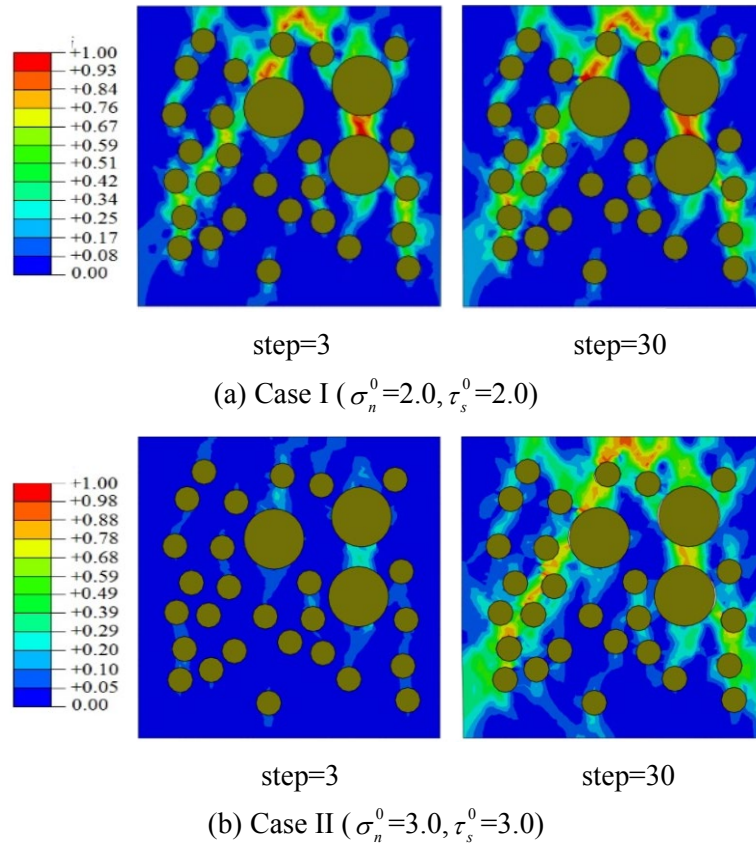


Figure 18: The equivalent positive damage distribution for uniaxial compression (different strength)

7 Conclusions

The initial defects in concrete, like the ITZ and the micro voids in mortar matrix, weaken the mechanical properties of concrete. To explore the weakening effect of the initial defects on the overall properties of concrete, the study carried out the research work of the constitutive law of material with defects and the numerical modeling on meso scale. Specifically, an elastic-damage traction-separation model for ITZ is developed and an anisotropic plastic-damage model for mortar matrix is modified by introducing the initial isotropic damage reflecting the weakening effect of defects. The FEM for concrete on meso scale is established by embedding the cohesive elements into the ITZ, and applied the proposed constitutive laws into corresponding components. The effectiveness of the proposed model has been verified by uniaxial tension and compression of concrete specimen. Finally, the effect of porosity, ITZ stiffness and strength on the mechanical properties of concrete are investigated, and some conclusions are drawn as follows

1) The peak stress and the energy release rate of concrete specimen decrease with the increase of porosity. That is to say, the more initial micro voids in concrete, the lower its strength and the more brittle the material is, whether under tension or compression.,

which is different from that of air-entrained concrete due to the resisting effect of the internal air press in voids.

2) The mechanical characteristics of ITZ reduce the overall properties of concrete material greatly when the ITZ strength is less than that of mortar matrix. What's more, the stiffness of ITZ can directly influence the strength and the damage distribution of concrete material. The large particles take on an inhibitory effect on the small one which causes the different damage development path for tension stress status. And the large aggregate takes on a shield effect on small one for compressive-shear stress status. So, the better mechanical properties of concrete would be obtained by only improving the mechanical behavior of ITZ on large aggregates.

3) Whether the ITZ strength is stronger or weaker than that of mortar matrix, the damage evolution path and failure mode of concrete material are influenced. When the normal strength of ITZ is less than the tension strength of mortar matrix, the damages firstly produce in ITZ, and develop to the mortar area from the particle boundary. However, the damages in mortar matrix always develop prior to ITZ once the normal strength of ITZ is improved to the same of tension strength of mortar matrix. It is worth noting that the damage strip is more concentrate in mortar matrix for the case of higher ITZ strength which results in failure of whole structure easily.

In this study, although the stochastic mechanical properties of concrete are reflected by the random distributed aggregates reforming to gradation rule of concrete, the stochastic features from the mortar matrix, the shape of aggregates and the ITZ have not been embodied. Further work in this area will be carried out in the framework of probabilistic sensitivity analysis [Vu-Bac, Lahmer, Zhuang et al. (2016); Hamdia, Silani, Zhuang et al. (2017)]. In addition, the multiscale mechanical characteristic of concrete has not been simulated completely, which can refer to the work of Hossein Talebi et al. [Talebi, Silani and Rabczuk (2015)] and Patabhi R. Budarapu et al. [Budarapu, Gracie, Yang et al. (2014)].

Acknowledgement: This work has been partially supported by National key research and development plan 13th Five-Year special item of China (2018YFC0406700, 2017YFC1502603) and the National Natural Science Foundation of China (Nos. 11672101, 51879260). Their financial support is gratefully acknowledged.

References

Al-Rub, R. A.; Voyiadjis, G. Z. (2006): A finite strain plastic-damage model for high velocity impact using combined viscosity and gradient localization limiters: Part I-theoretical formulation. *International Journal of Damage Mechanics*, vol. 15, no. 4, pp. 293-334.

Al-Rub, R. K. A.; Kim, S. M. (2010): Computational applications of a coupled plasticity-damage constitutive model for simulating plain concrete fracture. *Engineering Fracture Mechanics*, vol. 77, no. 10, pp. 1577-1603.

Al-Rub, R. K. A.; Voyiadjis, G. Z. (2003): On the coupling of anisotropic damage and plasticity models for ductile materials. *International Journal of Solids and Structures*, vol. 40, no. 11, pp. 2611-2643.

- Bažant, Z. P.; Tabbara, M. R.; Kazemi, M. T.; Pijaudier-Cabot, G.** (1990): Random particle model for fracture of aggregate or fiber composites. *Journal of Engineering Mechanics*, vol. 116, no. 8, pp. 1686-1705.
- Benzeggagh, M. L.; Kenane, M. J. C. S.** (1996): Measurement of mixed-mode delamination fracture toughness of unidirectional glass/epoxy composites with mixed-mode bending apparatus. *Composites Science and Technology*, vol. 56, no. 4, pp. 439-449.
- Budarapu, P. R.; Gracie, R.; Yang, S. W.; Zhuang, X. Y.; Rabczuk, T.** (2014): Efficient coarse graining in multiscale modeling of fracture. *Theoretical and Applied Fracture Mechanics*, vol. 69, pp. 126-143.
- Carol, I.; Prat, P. C.; Lopez, C. M.** (1997): Normal/shear cracking model: application to discrete crack analysis. *Journal of Engineering Mechanics*, vol. 123, no. 8, pp. 765-773.
- Chow, C. L.; Wang, J.** (1987): An anisotropic theory of elasticity for continuum damage mechanics. *International Journal of Fracture*, vol. 33, no. 1, pp. 3-16.
- Cicekli, U.; Voyiadjis, G. Z.; Al-Rub, R. K. A.** (2007): A plasticity and anisotropic damage model for plain concrete. *International Journal of Plasticity*, vol. 23, no. 10-11, pp. 1874-1900.
- Cusatis, G.; Mencarelli, A.; Pelessone, D.; Baylot, J.** (2011): Lattice discrete particle model (LDPM) for failure behavior of concrete. II: calibration and validation. *Cement and Concrete Composites*, vol. 33, no. 9, pp. 891-905.
- Cusatis, G.; Pelessone, D.; Mencarelli, A.** (2011): Lattice discrete particle model (LDPM) for failure behavior of concrete. I: theory. *Cement and Concrete Composites*, vol. 33, no. 9, pp. 881-890.
- Fang, N. Z.; Xia, X. Z.; Zhang, Q.** (2018): Extended finite element simulation of disconnection process in transition zone of concrete internal interface. *Journal of Wuhan University of Technology (Transportation Science & Engineering)*, vol. 42, no. 6, pp. 981-985, 991.
- Fang, Q.; Zhang, J. H.; Huan, Y.; Zhang, Y. D.** (2013): The investigation into three-dimensional mesoscale modelling of fully-graded concrete. *Engineering Mechanics*, vol. 30, no. 1, pp. 14-21.
- Ferté, G.; Massin, P.; Moës, N.** (2016): 3D crack propagation with cohesive elements in the extended finite element method. *Computer Methods in Applied Mechanics and Engineering*, vol. 300, pp. 347-374.
- Fu, G.; Dekelbab, W.** (2003): 3-D random packing of polydisperse particles and concrete aggregate grading. *Powder Technology*, vol. 133, no. 1-3, pp. 147-155.
- Gálvez, J. C.; Planas, J.; Sancho, J. M.; Reyes, E.; Cendón, D. A. et al.** (2013): An embedded cohesive crack model for finite element analysis of quasi-brittle materials. *Engineering Fracture Mechanics*, vol. 109, pp. 369-386.
- Hamdia, K. M.; Silani, M.; Zhuang, X. Y.; He, P. F.; Rabczuk, T.** (2017): Stochastic analysis of the fracture toughness of polymeric nanoparticle composites using polynomial chaos expansions. *International Journal of Fracture*, vol. 206, no. 2, pp. 215-227.
- Huang, Y.; Yang, Z.; Ren, W.; Liu, G.; Zhang, C.** (2015): 3D meso-scale fracture modelling and validation of concrete based on in-situ X-ray computed tomography

images using damage plasticity model. *International Journal of Solids and Structures*, vol. 67, pp. 340-352.

Idiart, A. E.; López, C. M.; Carol, I. (2011): Chemo-mechanical analysis of concrete cracking and degradation due to external sulfate attack: a meso-scale model. *Cement and Concrete Composites*, vol. 33, no. 3, pp. 411-423.

Kim, S. M.; Al-Rub, R. K. A. (2011): Meso-scale computational modeling of the plastic-damage response of cementitious composites. *Cement and Concrete Research*, vol. 41, no. 3, pp. 339-358.

Lilliu, G.; Van Mier, J. G. (2003): 3D lattice type fracture model for concrete. *Engineering Fracture Mechanics*, vol. 70, no. 7-8, pp. 927-941.

Lubliner, J.; Oliver, J.; Oller, S.; Onate, E. (1989): A plastic-damage model for concrete. *International Journal of Solids and Structures*, vol. 25, no. 3, pp. 299-326.

Mazars, J.; Pijaudier-Cabot, G. (1989): Continuum damage theory-application to concrete. *Journal of Engineering Mechanics*, vol. 115, no. 2, pp. 345-365.

Moës, N.; Belytschko, T. (2002): Extended finite element method for cohesive crack growth. *Engineering Fracture Mechanics*, vol. 69, no. 7, pp. 813-833.

Mura, T. (2013): *Micromechanics of Defects in Solids*. Springer Science & Business Media.

Nakamura, H.; Srisoros, W.; Yashiro, R.; Kunieda, M. (2006): Time-dependent structural analysis considering mass transfer to evaluate deterioration process of RC structures. *Journal of Advanced Concrete Technology*, vol. 4, no. 1, pp. 147-158.

Ollivier, J. P.; Maso, J. C.; Bourdette, B. (1995): Interfacial transition zone in concrete. *Advanced Cement Based Materials*, vol. 2, no. 1, pp. 30-38.

Rabczuk, T.; Belytschko, T. (2004): Cracking particles: a simplified meshfree method for arbitrary evolving cracks. *International Journal for Numerical Methods in Engineering*, vol. 61, no. 13, pp. 2316-2343.

Rabczuk, T.; Belytschko, T. (2007): A three-dimensional large deformation meshfree method for arbitrary evolving cracks. *Computer Methods in Applied Mechanics and Engineering*, vol. 196, no. 29-30, pp. 2777-2799.

Rabczuk, T.; Bordas, S.; Zi, G. (2010): On three-dimensional modelling of crack growth using partition of unity methods. *Computers and Structures*, vol. 88, no. 23-24, pp. 1391-1411.

Rabczuk, T.; Zi, G.; Bordas, S.; Nguyen-Xuan, H. (2008): A geometrically non-linear three-dimensional cohesive crack method for reinforced concrete structures. *Engineering Fracture Mechanics*, vol. 75, no. 16, pp. 4740-4758.

Rabczuk, T.; Zi, G.; Bordas, S.; Nguyen-Xuan, H. (2010): A simple and robust three-dimensional cracking-particle method without enrichment. *Computer Methods in Applied Mechanics and Engineering*, vol. 199, no. 37-40, pp. 2437-2455.

Schlangen, E.; Garboczi, E. J. (1997): Fracture simulations of concrete using lattice models: computational aspects. *Engineering Fracture Mechanics*, vol. 57, no. 2-3, pp. 319-332.

Simo, J. C.; Ju, J. W. (1987): Strain-and stress-based continuum damage models-I. Formulation. *International Journal of Solids and Structures*, vol. 23, no. 7, pp. 821-840.

Simo, J. C.; Ju, J. W. (1987): Strain-and stress-based continuum damage models-II. Computational aspects. *International Journal of Solids and Structures*, vol. 23, no. 7, pp. 841-869.

Su, X. T.; Yang, Z. J.; Liu, G. H. (2010): Finite element modelling of complex 3D static and dynamic crack propagation by embedding cohesive elements in Abaqus. *Acta Mechanica Solida Sinica*, vol. 23, no. 3, pp. 271-282.

Sun, L. G. (2005): Numerical simulation of shape of aggregates of three-graded concrete (full-graded concrete) and application. *Dissertation for Master Degree of Science*, Hohai University, China.

Talebi, H.; Silani, M.; Bordas, S. P. A.; Kefriden, P.; Rabczuk, T. (2014): A computational library for multiscale modeling of material failure. *Computational Mechanics*, vol. 53, no. 5, pp. 1047-1071.

Talebi, H.; Silani, M.; Rabczuk, T. (2015): Concurrent multiscale modeling of three dimensional crack and dislocation propagation. *Advances in Engineering Software*, vol. 80, pp. 82-92.

Van Mier, J. G. (2017): *Fracture Processes of Concrete*. CRC Press.

Voyiadjis, G. Z. (2012): *Advances in Damage Mechanics: Metals and Metal Matrix Composites*. Elsevier.

Voyiadjis, G. Z.; Al-Rub, R. A.; Palazotto, A. N. (2003): Non-local coupling of viscoplasticity and anisotropic viscodamage for impact problems using the gradient theory. *Archives of Mechanics*, vol. 55, no. 1, pp. 40-90.

Voyiadjis, G. Z.; Al-Rub, R. A.; Palazotto, A. N. (2004): Thermodynamic framework for coupling of non-local viscoplasticity and non-local anisotropic viscodamage for dynamic localization problems using gradient theory. *International Journal of Plasticity*, vol. 20, no. 6, pp. 981-1038.

Voyiadjis, G. Z.; Park, T. (1997): Anisotropic damage effect tensors for the symmetrization of the effective stress tensor. *Journal of Applied Mechanics*, vol. 64, no. 1, pp. 106-110.

Vu-Bac, N.; Lahmer, T.; Zhuang, X.; Nguyen-Thoi, T.; Rabczuk, T. (2016): A software framework for probabilistic sensitivity analysis for computationally expensive models. *Advances in Engineering Software*, vol. 100, pp. 19-31.

Wang, X. F.; Yang, Z. J.; Jivkov, A. P. (2015): Monte Carlo simulations of mesoscale fracture of concrete with random aggregates and pores: a size effect study. *Construction and Building Materials*, vol. 80, pp. 262-272.

Wischers, G. (1978): Application of effects of compressive loads on concrete. *Betontechnische Berichte*, no. 2, pp. 103-115.

Yan, D. M. (2006): *Experiment and Theoretical Study on the Dynamic Properties of Concrete (Ph.D. Thesis)*. Dalian University of Technology, China.

Yin, A. Y.; Yang, X. H.; Yang, Z. J. (2013): 2D and 3D fracture modeling of asphalt mixture with randomly distributed aggregates and embedded cohesive cracks. *Procedia IUTAM*, vol. 6, pp. 114-122.

Zhu, W. C.; Tang, C. A. (2002): Numerical simulation on shear fracture process of concrete using mesoscopic mechanical model. *Construction and Building Materials*, vol. 16, no. 8, pp. 453-463.

Zhu, W. C.; Teng, J. G.; Tang, C. A. (2004): Mesomechanical model for concrete. Part I: model development. *Magazine of Concrete Research*, vol. 56, no. 6, pp. 313-330.

Zhuo, J. S.; Zhang, Q. (2000): *Interfacial Element Method for Discontinuous Medium Mechanics*. Science Press, Beijing.